Monthly Notices of the ROYAL ASTRONOMICAL SOCIETY

MNRAS **548,** 1–16 (2026) https://doi.org/10.1093/mnras/stag810
Advance Access publication 2026 April 30

MIGHTEE-H I: the star-forming properties of H I-selected galaxies

Madalina N. Tudorache [1★] M. J. Jarvis [1,2] A. A. Ponomareva [1,3] I. Heywood,[1,4,5] N. Maddox [6] M. Glowacki [7,8] B. S. Frank,[5,8,9,10] M. Baes [11] R. Davé [2,7] S. L. Jung [1] M. Maksymowicz-Maciata,[6] H. Pan [1] and K. Spekkens[12]

[1]*Astrophysics, Department of Physics, University of Oxford, Keble Road, Oxford OX1 3RH, UK*
[2]*Department of Physics and Astronomy, University of the Western Cape, Robert Sobukwe Road, 7535 Bellville, Cape Town, South Africa*
[3]*Centre for Astrophysics Research, School of Physics, Astronomy and Mathematics, University of Hertfordshire, College Lane, Hatfield AL10 9AB, UK*
[4]*Department of Physics and Electronics, Rhodes University, PO Box 94, Makhanda 6140, South Africa*
[5]*South African Radio Astronomy Observatory, 2 Fir Street, Black River Park, Observatory, Cape Town 7925, South Africa*
[6]*School of Physics, H.H. Wills Physics Laboratory, Tyndall Avenue, University of Bristol, Bristol BS8 1TL, UK*
[7]*Institute for Astronomy, University of Edinburgh, Royal Observatory, Edinburgh EH9 3HJ, UK*
[8]*The Inter-University Institute for Data Intensive Astronomy (IDIA), Department of Astronomy, University of Cape Town, Private Bag X3, Rondebosch 7701, South Africa*
[9]*STFC UK Astronomy Technology Centre, Royal Observatory, Edinburgh, Blackford Hill, Edinburgh EH9 3HJ, UK*
[10]*Department of Astronomy, University of Cape Town, Private Bag X3, Rondebosch 7701, South Africa*
[11]*Sterrenkundig Observatorium, Universiteit Gent, Krijgslaan 281 S9, B-9000 Gent, Belgium*
[12]*Department of Physics, Engineering Physics & Astronomy, Queen's University, Kingston, ON K7L 3N6, Canada*

Accepted 2026 April 28. Received 2026 April 28; in original form 2024 November 25

ABSTRACT

The interplay between atomic gas and the star formation history (SFH) of a galaxy are intrinsically linked, and we need to decouple these dependencies to understand their role in galaxy formation and evolution. In this paper, we analyse the SFH of 203 galaxies from the MIGHTEE-H I Survey Early Science Release data, cross-matched to with multiwavelength photometry across the COSMOS and XMM-LSS fields. We focus on the relationships between H I properties and star formation, with a sample which primarily traces gas-rich, star-forming systems at low redshift, extending to low stellar masses and probing regimes that are difficult to access with optically selected samples. A strong correlation emerges between a galaxy's H I-to-stellar mass ratio and the time of formation, alongside an inverse correlation between stellar mass and time of formation, regardless of the inferred SFH. Additionally, galaxies with lower stellar masses and higher H I-to-stellar mass ratios exhibit longer gas depletion times compared to more massive galaxies, which appear to have depleted their gas and formed stars more efficiently. This suggests that smaller, gas-rich galaxies have higher depletion times due to shallower potential wells and less efficient star formation. Within this H I-selected sample, the efficiency of star formation is regulated primarily by stellar mass and gas fraction, with low-mass galaxies retaining extended atomic reservoirs due to inefficient conversion of H I into stars.

Key words: galaxies: evolution – galaxies: formation – galaxies: kinematics and dynamics.

1 INTRODUCTION

There is a bimodality in the population of galaxies: there are blue, younger, star-forming galaxies and red, quenched galaxies (J. Kennicutt 1998; I. Strateva et al. 2001; I. K. Baldry et al. 2004; M. L. Balogh et al. 2004; C. F. McKee & E. C. Ostriker 2007; R. C. Kennicutt & N. J. Evans 2012). The processes involved in how galaxies stop forming stars are complex and there has been a lot of effort devoted to understand what processes lead to the quenching of galaxies, leading them to move from the blue cloud to the red sequence. From feedback processes – due to both supernovae (J. Silk & G. A. Mamon 2012; P. F. Hopkins et al. 2014) and active galactic nuclei (T. Di Matteo, V. Springel & L. Hernquist 2005; A. King 2005; D. J. Croton et al. 2006; A. C. Fabian 2012) – to mergers (J. E. Barnes & L. E. Hernquist 1991; C. Lacey & S. Cole 1993) and environmental processes, there are many effects that need to be taken into account to understand how galaxies depart from the star-forming (SF) main sequence (MS), which links the stellar mass of a galaxy and its star formation activity (K. G. Noeske et al. 2007; K. E. Whitaker et al. 2012; R. Johnston et al. 2015; P. Popesso et al. 2019a, b; S. K. Leslie et al. 2020; A. Fraser-McKelvie et al. 2021; J. E. Thorne et al. 2021). Whilst the overall shape of the MS is generally agreed on, such that it increases up to a knee mass and then flattens before the star formation rate (SFR) drops precipitously (S. J. Lilly et al. 2013; K. E. Whitaker et al. 2014; P. Popesso et al. 2019b), its scatter is less understood (K. E. Whitaker et al. 2015; J. Matthee & J. Schaye 2019).

★ E-mail: madalina.tudorache@physics.ox.ac.uk

The star formation history (SFH) encodes the temporal narrative of a galaxy's star formation activity. Inferring SFHs involves deciphering the distribution of stellar ages, shedding light on the intensity and duration of past star-forming epochs, potentially providing insights into the physical mechanisms that terminate star formation (e.g. C. Schreiber et al. 2018). Similarly, the SFHs of star-forming galaxies can give us information about the assembly of their stellar masses (e.g. S. N. Leitner 2012). The study of stellar populations through colour–magnitude diagrams, spectroscopy, and sophisticated modelling techniques can contribute to disentangling the complex interplay of factors influencing star formation, such as gas availability, environmental conditions, and feedback processes (P. Ocvirk et al. 2006; S. Dye 2008; J. Leja et al. 2017, 2019; S. Tacchella et al. 2022).

Tying everything together, there are several prevailing theories that aim to explain the scatter in the MS, related to the SFH of a galaxy. Variations in SFHs, driven by episodic or bursty star formation, lead to deviations from the SF MS as galaxies experience different phases of heightened or suppressed star formation (K. Finlator & R. Davé 2008; S. J. Lilly et al. 2013; A. Dekel & N. Mandelker 2014; S. Tacchella et al. 2016). These fluctuations are closely tied to the dynamics of gas flows, where inflows of cold gas replenish the fuel for star formation, causing temporary surges in SFRs that push galaxies above the SF MS. On the other hand, outflows driven by feedback mechanisms like stellar winds and active galactic nuclei (AGNs) can deplete the gas reservoir, reducing SFRs and causing galaxies to fall below the sequence. The balance between these gas inflows and outflows, along with the efficiency of gas conversion into stars, contributes to the diversity of SFHs and the resulting scatter around the SF MS (L. E. Abramson et al. 2015; J. A. Muñoz & M. S. Peeples 2015). However, there are cases in which the SFH variations do not necessarily have any dramatic bursts or quenching events, such that their offset from the MS is a long time-scale effect (A. Rodríguez-Puebla et al. 2016; J. Matthee & J. Schaye 2019). These galaxies might be in environments that slowly strip away their gas, such as in galaxy clusters where processes like ram pressure stripping or strangulation gradually remove the cold gas needed for star formation. Then, over time, this slow decline in gas content leads to a reduction in SFRs, causing these galaxies to drift below the SF MS while maintaining a stable, but uneventful SFH (Y.-j. Peng et al. 2010; P. S. Behroozi, R. H. Wechsler & C. Conroy 2013). Hence, if the MS scatter arises from short-term fluctuations, star-forming galaxies with similar masses mostly grew self-similarly. However, if the scatter in the MS arises due to longer-term fluctuations, then star-forming galaxies with similar mass may not have evolved in a similar way and the key physical mechanisms lie in the processes that diversify the SFHs.

For this study, we use an H I galaxy sample provided by the MeerKAT International GigaHertz Tiered Extragalactic Exploration (MIGHTEE, M. Jarvis et al. 2016) Early Science release to investigate the SFHs of an H I-selected sample. The H I selection provides a sample of galaxies that have the most prevalent reservoir of cold neutral gas, which is required for the molecular gas to form and result in *in-situ* star formation.

We assume ΛCDM cosmology with $H_0 = 70\ \mathrm{km\,s^{-1}\,Mpc^{-1}}$ and $\Omega_\mathrm{M} = 0.3$ and $\Omega_\Lambda = 0.7$. The structure of this paper is organized as follows. Section 2 introduces the data used in this study and the process of fitting of spectral energy distributions to infer the galaxy properties. Section 3 discusses the results obtained. The summary and conclusions are presented in Section 4.

Table 1. Summary of the MIGHTEE-H I Early Science data products used in this paper.

Area covered	$\sim 1\,\mathrm{deg^2}$ COSMOS field
	$\sim 3\,\mathrm{deg^2}$ XMM-LSS field
Frequency range	1320 − 1410 MHz
Redshift range	0.004 − 0.084
Channel width	209 kHz
Median $\mathrm{H_I}$ channel rms noise	85 μJy beam^{-1}
N_HI sensitivity (3σ)	1.6×10^{20} cm^{-2} (per channel)
Synthesized beam	$14.5''x11''$ COSMOS field
	$12''x10''$ XMM-LSS field

2 DATA

2.1 The MIGHTEE survey

The MIGHTEE survey is one of eight Large Survey Projects using MeerKAT (J. L. Jonas 2009). MeerKAT comprises a configuration of 64 offset-Gregorian dishes, each featuring a main reflector with a 13.5 m diameter and a sub-reflector with a 3.8 m diameter. The receivers for MeerKAT operate across three bands: *UHF* band ($580 < \nu < 1015$ MHz), *L* band ($900 < \nu < 1670$ MHz), and *S* band ($1750 < \nu < 3500$ MHz), all capable of collecting data in spectral-line mode. The MIGHTEE survey focuses on three main aspects: radio continuum (I. Heywood et al. 2021; C. L. Hale et al. 2024), polarization (A. R. Taylor et al. 2024), and spectral line (I. Heywood et al. 2024).

MIGHTEE-H I (N. Maddox et al. 2021) constitutes the H I emission project within the MIGHTEE survey. Data products, released as part of the Early Science phase, were provided using the `ProcessMeerKAT` calibration pipeline (J. D. Collier et al. 2021). This pipeline, based on `CASA` [1] (J. P. McMullin et al. 2007), operates in a parallelized manner and follows standard calibration routines such as flagging, delay, bandpass, and complex gain calibration. Spectral-line imaging is performed using `CASA`'s `TCLEAN` task. Continuum subtraction was executed in two domains. Visibility domain subtraction utilized standard `CASA` routines, namely `UVSUB` and `UVCONTSUB`. Subsequently, image plane-based continuum subtraction was implemented through per-pixel median filtering, applied to the resulting data cubes to mitigate the impact of direction-dependent artefacts. The summary of the data utilized in this paper is provided in Table 1. In this study, we specifically utilize the spectral line data from the *L*-band Early Science (see A. A. Ponomareva et al. 2023, for source catalogues), employing 4096 channels with a channel width of 209 kHz, corresponding to a velocity resolution of 44 km s^{-1} at redshift $z = 0$. These observations cover two of the four MIGHTEE fields, namely COSMOS and XMM-LSS, where we have excellent multiwavelength ancillary data to determine the properties of H I-selected galaxies from MIGHTEE. The sample of galaxies reaches much lower H I gas masses at a given redshift than previous wide-area single dish surveys (e.g. M. J. Meyer et al. 2007; M. P. Haynes et al. 2011), while the fields covered provide access to the deepest and largest spectral coverage to estimate the stellar properties of the galaxies and, as we will show in Section 3, reach stellar masses as low as $M_\star \sim 10^{7.5}\,\mathrm{M_\odot}$. Furthermore, the high angular resolution means that confusion between sources, which can lead to over-estimates of the H I mass from single-dish surveys, is negated.

[1] http://casa.nrao.edu

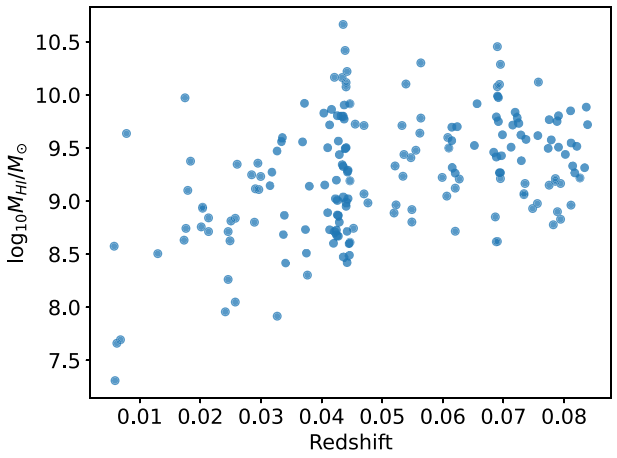

Figure 1. Atomic gas mass $M_{\rm HI}$ as a function of redshift for the MIGHTEE-H I Early Release Science catalogue used in this work.

There are 276 galaxies in the full Early Science H I catalogue. We cross-matched these galaxies with the Deep Extragalactic VIsible Legacy Survey (DEVILS; L. J. M. Davies et al. 2018) photometric catalogue (L. J. M. Davies et al. 2021), in order to obtain ultraviolet through to mid- and far-infrared data measured in a consistent way using ProFOUND (A. S. G. Robotham et al. 2018). The DEVILS photometric catalogue is derived from the imaging data using the *Galaxy Evolution Explorer* (GALEX; M. A. Zamojski et al. 2007) for ultraviolet wavelengths, the Canada–France–Hawaii Telescope (CFHT; O. Ilbert et al. 2006; P. Capak et al. 2007) (*u* band), HyperSuprimeCam (HSC; H. Aihara et al. 2019) (*grizy*), Visible-Infrared Survey Telescope for Astronomy (VISTA; H. J. McCracken et al. 2012; M. J. Jarvis et al. 2013) ($YJHK_s$), *Spitzer Space Telescope* (C. J. Lonsdale et al. 2003; D. B. Sanders et al. 2007; J. C. Mauduit et al. 2012) (mid-infrared, IRAC ch1-ch4 and MIPS 24 μm, 70 μm), and the *Herschel Space Observatory* (S. J. Oliver et al. 2012) (far-infrared, PACS and SPIRE). This plethora of very deep imaging data from the UV through to the far-infrared allows us to perform galaxy SED fitting to much better accuracy than has been possible for H I-selected samples. Importantly, by sampling both the rest frame UV and far-infrared emission, we are sensitive to the total SFR in these galaxies.

However, some of the galaxies do not have full photometry available due to the MIGHTEE Early Science Release data extending beyond the slightly smaller areal coverage of the optical and near-infrared data, reducing the sample to 203 galaxies. This does not introduce any extra selection effects in the data, as the galaxies are purely excluded due to the footprint of the DEVILS survey (see fig. 1 of R. H. W. Cook et al. 2024). Fig. 1 shows the distribution of their H I mass as a function of redshift.

2.2 SED fitting of galaxies

There are several different algorithms that can be used for fitting spectral energy distributions (SEDs) of galaxies in order to obtain physical information from photometric data (e.g. O. Ilbert et al. 2006; J. Leja et al. 2017; A. S. G. Robotham et al. 2020). Known as template fitting, it involves fitting observed photometric data with theoretical templates or model spectra (M. Bolzonella, J. M. Miralles & R. Pelló 2000; O. Ilbert et al. 2006; J. Walcher et al. 2011; L. K. Hunt et al. 2019; C. Pacifici et al. 2023).

Table 2. A description of each of the parameters used for the exponentially delayed SFH model, as well as the priors used to fit the model. The parameters are (from top to bottom): the age of the galaxy, the SFR e-folding time τ, the stellar mass of the galaxy $M_\star$, the metallicity Z in units of solar metallicity, Z_0), the dust attenuation coefficient A_V, the PAH mass fraction $q_{\rm PAH}$, the lower limit of starlight intensity distribution $u_{\rm min}$, the fraction of stars at $u_{\rm min}$ γ and the ionization parameter, U.

Parameter	Prior distribution
Age	Uniform $\in$ [0.1, 15.0]
τ	Uniform $\in$ [0.3, 10.0]
$\log_{10} M_\star/M_\odot$	Uniform $\in$ [1.0, 15.0]
$\log_{10} Z/Z_\odot$	Uniform $\in$ [0.0, 2.5]
A_V	Uniform $\in$ [0.0, 3.0]
$q_{\rm PAH}$	Uniform $\in$ [0.1, 4.58]
$u_{\rm min}$	Uniform $\in$ [0.1, 20.0]
γ	Uniform $\in$ [0.0, 0.5]
$\log_{10} U$	Uniform $\in$ [−4.0, −1.0]

In this paper, we use BAGPIPES[2] (A. C. Carnall et al. 2018), which is a PYTHON tool that uses Bayesian inference to fit model SEDs to measured galaxy SEDs and provide redshifts and galaxy properties using spectroscopic and/or photometric data from the ultraviolet to the microwave regime. BAGPIPES provides a framework for computing both parametric and non-parametric SFHs, such as delta functions, constant, exponentially declining, delayed exponentially declining, log-normal, double-power law or any custom input (see A. C. Carnall et al. 2018 for all the functional forms). For our sample of galaxies, given that we already have redshifts (from both DEVILS and H I measurements), we fix the redshift values and run BAGPIPES with the G. Bruzual & S. Charlot (2003) stellar population model, which is characterized by a G. Chabrier (2003) IMF. For dust, we apply the D. Calzetti et al. (2000) attenuation law with priors on E(B-V) = (0.0, 3.0). We also apply the J. A. Cardelli, G. C. Clayton & J. S. Mathis (1989) attenuation law with similar priors. However, we only show the results of the D. Calzetti et al. (2000) attenuation law, as the trends do not change. The dust emission from the neutral ISM is modelled as a single-temperature grey-body (R. H. Hildebrand 1983). Similarly, we use uniform priors for all other properties (Table 2). An example of the fit can be seen in Fig. 2. Examples of fits for other galaxies (as well as corner plots) can be seen in Appendix A, in Figures A1 and A2.

In Bayesian inference, the statistical distribution of a set of parameters, $\boldsymbol{\theta}$, for a model $\mathcal{M}$, given some data, $\boldsymbol{d}$, is given by Bayes theorem:

$$\mathcal{P}(\boldsymbol{\theta}|\boldsymbol{d},\mathcal{M}) = \frac{\mathcal{L}(\boldsymbol{d}|\boldsymbol{\theta},\mathcal{M})\Pi(\boldsymbol{\theta}|\mathcal{M})}{\mathcal{Z}(\boldsymbol{d}|\mathcal{M})}, \quad (1)$$

where $\mathcal{P}(\boldsymbol{\theta}|\boldsymbol{d},\mathcal{M})$ is the posterior probability, $\mathcal{L}(\boldsymbol{d}|\boldsymbol{\theta},\mathcal{M})$ is the likelihood, $\Pi(\boldsymbol{\theta}|\mathcal{M})$ represents the priors and $\mathcal{Z}(\boldsymbol{d}|\mathcal{M})$ is the evidence. As BAGPIPES uses a Bayesian inference approach to compute the SFHs and the stellar masses, we can also use the evidence ($\log \mathcal{Z}(\boldsymbol{d}|\mathcal{M}_i)$) for each model i and for each galaxy. We can then use the Bayes factor and the Jeffreys scale (H. Jeffreys 1998) to verify which model is preferred accounting for model complexity. We define the Bayes' factor as

$$\log B_{01} \equiv \log \mathcal{Z}(\boldsymbol{d}|\mathcal{M}_0) - \log \mathcal{Z}(\boldsymbol{d}|\mathcal{M}_1), \quad (2)$$

[2] http://bagpipes.readthedocs.io

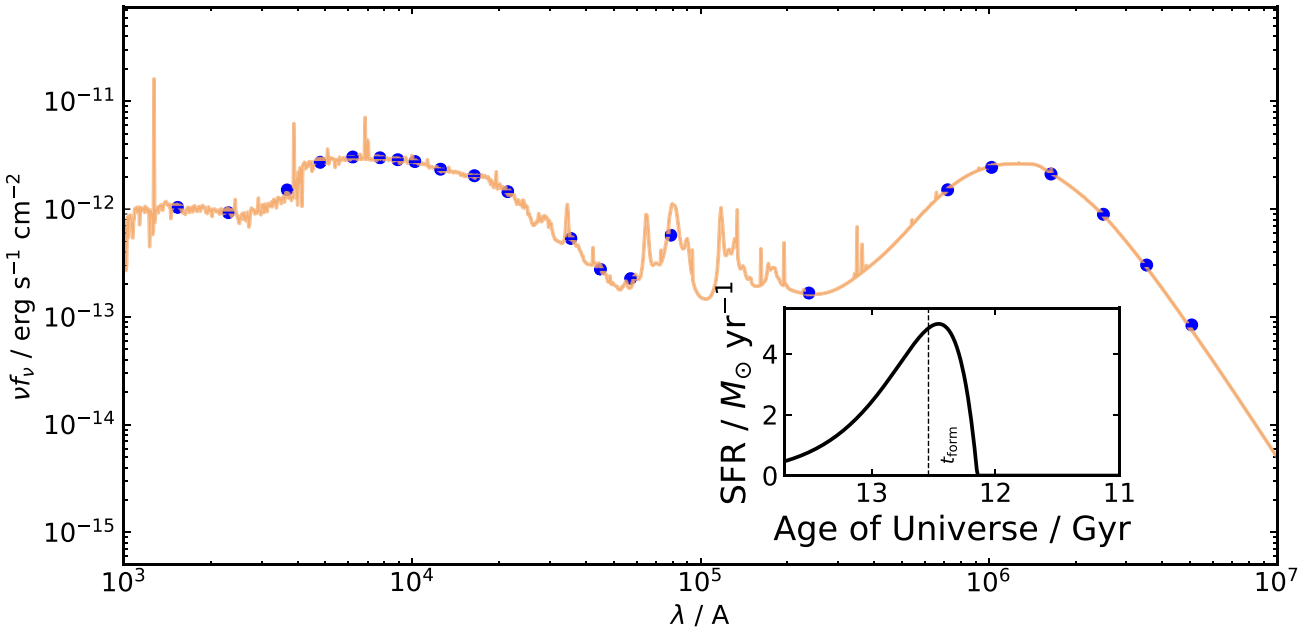

Figure 2. An example of the photometric output of one of the MIGHTEE-H I Early Science galaxies using the available photometric filters, fitted with an exponentially delayed SFH (presented as an inset in the bottom right corner, along with a dashed vertical line showing $t_{\rm form}$). This is a galaxy with SFR $= 0.54$ M$_\odot$/yr, $M_\star = 10^{9.38}$ M$_\odot$ and $M_{\rm HI} = 10^{8.98}$ M$_\odot$.

where $\mathcal{M}_0$ and $\mathcal{M}_1$ are two models which we are comparing. We take $\log B_{01} < 1$ as 'not significant', $1 < \log B_{01} < 2.5$ as 'significant', $2.5 < \log B_{01} < 5$ as 'strong', and $\log B_{01} > 5$ as 'decisive' (H. Jeffreys 1998) as a way to determine the preferred model given the data and number of free parameters.

3 RESULTS AND DISCUSSION

3.1 Galaxy SED models

As described in Section 2.2, BAGPIPES provides many models that can be fit to a galaxy in order to infer its SFH. We use the six available parametric SFH models for our galaxy sample: the exponential SFH, the constant SFH, the log-normal SFH, the delayed SFH, the burst SFH and the double-power law SFH. To compare the SFH models from BAGPIPES, we use the Bayesian framework described in Section 2.2. We calculate the Bayes' factor for each galaxy and for each model and proceed to draw a comparison between them. When comparing the SFH models for each galaxy, we find that the broadband data is not sufficient to differentiate between the exponential SFH, the lognormal SFH and the exponentially delayed SFH model.

Furthermore, we also use the BAGPIPES implementation of the non-parametric model of J. Leja et al. (2019). As for the parametric model case, the Bayesian evidence suggests that we cannot differentiate which is preferred between the non-parametric and the exponentially delayed models, given our current data.

Therefore, for the rest of this paper we will only show the full results for the exponentially delayed SFH model. For reference, the exponentially delayed SFH model is defined as

$$\mathrm{SFR}(t) \propto \begin{cases} e^{-\frac{t-T_0}{\tau}} & t > T_0 \\ 0 & t < T_0 \end{cases}, \quad (3)$$

where τ is the SFR e-folding time and T_0 is the cosmic time.

However, we will show the relevant figures for the non-parametric model, where it differs from the parametric one. When presenting the correlation tests, we provide results for both models and highlight any differences where they occur.

3.2 The stellar properties of H I-selected galaxies

The processes involved in the conversion of H I to stars are complex and not well understood (N. Maddox et al. 2021). In the following, we investigate links between the H I-selected galaxy sample and several parameters which describe star formation. It should be noted that all the results presented below are in the context of an H I-selected sample, which provides unique insights into the most gas-rich systems. However, the fact that a galaxy must have significant amounts of H I in order to be detected means that the effect of low-mass H I galaxies on these relations will not be observed. This then also leads to being biased towards a sample formed of mostly spiral and irregular galaxies. Furthermore, galaxies with higher H I content are often actively forming stars, leading to a bias towards younger stellar populations, and galaxies on the MS. However, we are sensitive to low-luminosity dwarf galaxies, which tend to be gas-dominated (M. Geha et al. 2006) and not biased towards high surface brightness galaxies. Conversely to many optically selected samples used to investigate the dependence on H I, we are not significantly constrained by the luminosity of the stellar population, stellar mass, or dust extinction (J. F. Helmboldt et al. 2004; J. L. Rosenberg, S. E. Schneider & J. Posson-Brown 2005; S. Huang et al. 2012; A. M. Martin et al. 2012), as the multiwavelength data is very deep for the H I-selected galaxies at these very low ($z < 0.08$) redshifts (e.g. see N. J. Adams et al. 2021; L. J. M. Davies et al. 2021, for

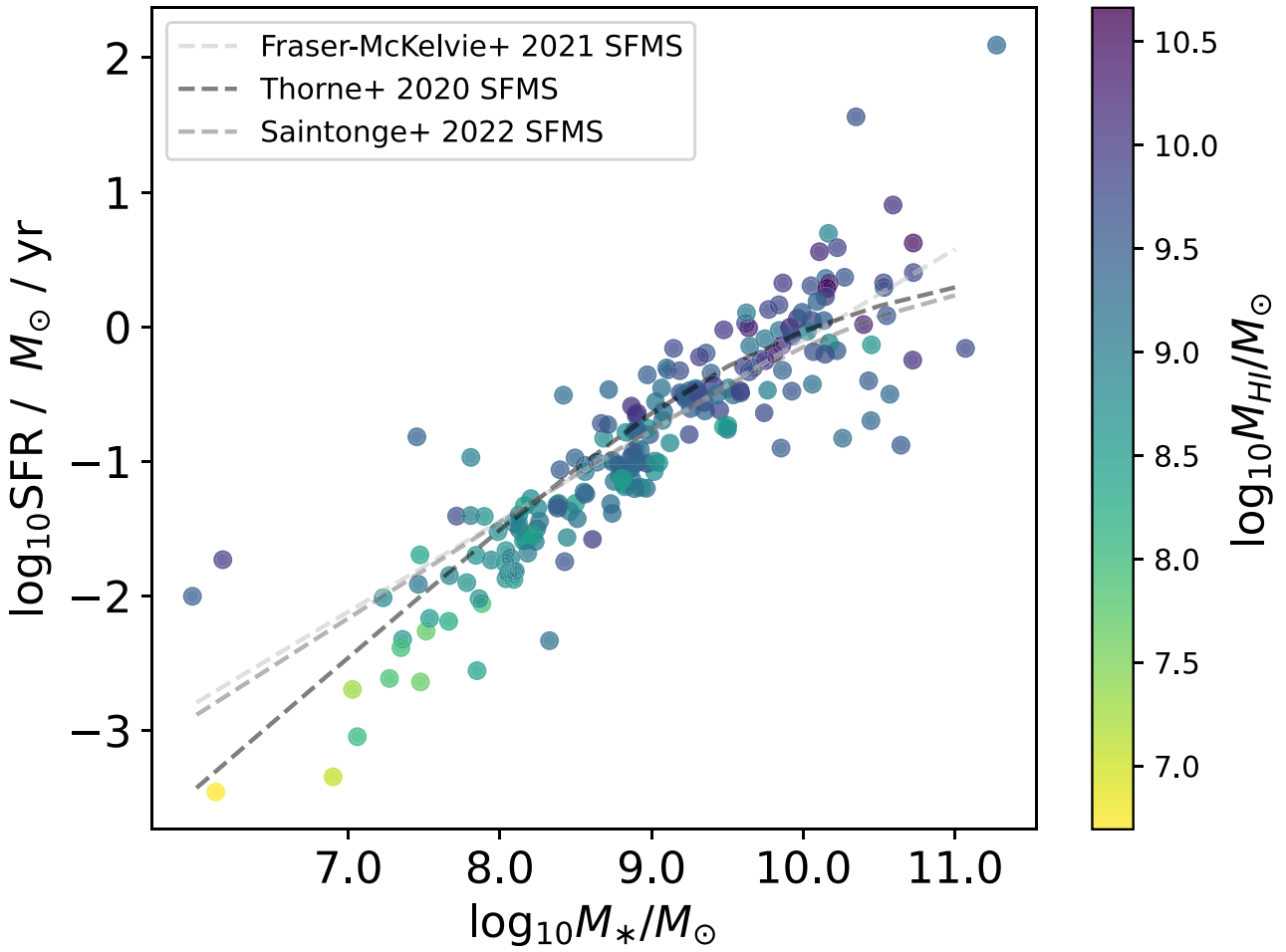

Figure 3. The stellar mass versus star formation for our H I-selected galaxies, with the properties derived from the best-fitting model using BAGPIPES. The H I mass is denoted by the colour bar. It is clear that the H I-selected results in a sample of galaxies that lie on the MS of star-forming galaxies, albeit with the often-seen turnover in star formation for the more massive galaxies in the sample showing that quenched galaxies may still retain a significant H I reservoir. The three dashed lines are different SF-MS fits: the black line is the SF MS as presented in J. E. Thorne et al. (2021), the light grey line is the linear SF MS as presented in A. Fraser-McKelvie et al. (2021) and the dark grey line is the SF MS as presented in A. Saintonge & B. Catinella (2022). All the SF–MS relations presented are computed from optically selected samples, and not an H I-selected sample.

more information). In Fig. 3, we show the stellar mass versus SFR for our H I-selected galaxies. This demonstrates that our galaxies are predominantly the H I-rich galaxies lying along or above the MS of star formation. However, we also find significant H I gas reservoirs ($M_{\rm HI} > 10^9$ M$_\odot$) in the more massive galaxies that are beginning to turn off the MS.

In the following sections, we discuss the relationship between the H I and the derived properties from the SED fitting with BAGPIPES. Full details of the derived parameters are given in Table 3 alongside the redshift from the H I line.

3.2.1 *The star formation history of H I-selected galaxies*

First, we investigate the H I mass as a function of the time of formation, $t_{\rm form}$ (measured forwards from the beginning of the Universe), which is defined as

$$\frac{\int_0^{t_{\rm obs}} t\,{\rm SFR}(t){\rm d}t}{\int_0^{t_{\rm obs}} {\rm SFR}(t){\rm d}t} = t(z_{\rm form}), \quad (4)$$

where $t_{\rm obs} \equiv t(z_{\rm obs})$, which is the redshift at which we observe the galaxies, and SFR is the star formation rate (A. C. Carnall et al. 2018).

As can be seen in Fig. 4, we do not find a trend between the time since the peak of the star formation in the galaxy and its H I mass. This is confirmed using Kendall's tau (M. G. Kendall 1938) and Spearman rank (G. J. Glasser & R. F. Winter 1961) tests for the exponentially delayed model (Table 4, left). For the case of the non-parametric SFH model, we find a weak anticorrelation, which is statistically much stronger (Table 4, right). On the other hand, Fig. 5 shows the time of formation against the H I-to-stellar mass ratio and here we see a positive correlation between the two parameters. This is also confirmed by the two correlation tests, shown in Table 4, irrespective of the SFH model (parametric or non-parametric).

As $M_{\rm HI}$ does not show a correlation with the time of formation, $t_{\rm form}$, but $M_{\rm HI}/M_\star$ does, we also investigate if there is any relationship between the stellar mass of a galaxy $M_\star$ and the time of formation $t_{\rm form}$. As can be seen in Fig. 6, there is an anticorrelation

Table 3. An excerpt of fitted parameters for the exponentially delayed model on the MIGHTEE-H I galaxies, as well as the H I mass. The full table is available as supplementary material.

ID	RA	Dec.	z	$\log_{10} M_{\rm HI}/M_\odot$	$\log_{10} M_\star/M_\odot$	SFR	sSFR	$t_{\rm form}$	$t_{\rm dep}$
0	150.4742	2.4137	0.0068	7.69	$7.29^{+0.001}_{-0.001}$	$0.007^{+0.001}_{-0.001}$	$-9.456^{+0.001}_{-0.001}$	$12.491^{+0.001}_{-0.001}$	$9.86^{+0.001}_{-0.001}$
1	150.613	2.1668	0.0059	7.31	$6.912^{+0.001}_{-0.001}$	$0.004^{+0.001}_{-0.001}$	$-9.269^{+0.001}_{-0.001}$	$12.522^{+0.001}_{-0.001}$	$9.666^{+0.001}_{-0.001}$
2	150.1253	2.1496	0.0041	6.69	$6.155^{+0.0}_{-0.0}$	$0.001^{+0.001}_{-0.001}$	$-9.454^{+0.001}_{-0.001}$	$12.59^{+0.001}_{-0.001}$	$9.994^{-0.001}_{-0.001}$
3	149.6951	2.3475	0.0058	8.57	$7.342^{+0.001}_{-0.001}$	$0.005^{+0.001}_{-0.001}$	$-9.652^{+0.003}_{-0.003}$	$12.433^{+0.002}_{-0.002}$	$10.884^{+0.003}_{-0.003}$
4	149.8662	2.007	0.013	8.51	$7.425^{+0.003}_{-0.003}$	$0.016^{+0.001}_{-0.001}$	$-9.232^{+0.004}_{-0.004}$	$11.823^{+0.020}_{-0.025}$	$10.313^{+0.001}_{-0.001}$
5	150.0243	1.911	0.0062	7.66	$7.47^{+0.002}_{-0.002}$	$0.002^{+0.001}_{-0.001}$	$-10.084^{+0.002}_{-0.003}$	$11.877^{+0.013}_{-0.013}$	$10.275^{+0.002}_{-0.001}$
6	150.5946	2.4223	0.0213	8.84	$7.963^{+0.001}_{-0.001}$	$0.026^{+0.001}_{-0.001}$	$-9.554^{+0.001}_{-0.001}$	$12.025^{+0.002}_{-0.002}$	$10.433^{+0.001}_{-0.001}$
7	149.812	2.192	0.0246	8.26	$7.447^{+0.001}_{-0.001}$	$0.009^{+0.001}_{-0.001}$	$-9.51^{+0.002}_{-0.002}$	$12.066^{+0.001}_{-0.001}$	$10.325^{+0.003}_{-0.001}$
8	150.3455	1.7935	0.0249	8.63	$7.843^{+0.0}_{-0.0}$	$0.031^{+0.001}_{-0.001}$	$-9.356^{+0.001}_{-0.001}$	$12.241^{+0.001}_{-0.001}$	$10.139^{+0.001}_{-0.001}$
9	150.5468	2.0216	0.0213	8.71	$9.061^{+0.002}_{-0.002}$	$0.087^{+0.001}_{-0.001}$	$-10.122^{+0.002}_{-0.002}$	$10.952^{+0.017}_{-0.019}$	$9.774^{+0.001}_{-0.001}$
10	149.9643	1.7067	0.025	8.81	$7.204^{+0.001}_{-0.001}$	$0.016^{+0.001}_{-0.001}$	$-9.003^{+0.001}_{-0.001}$	$12.569^{+0.001}_{-0.001}$	$10.612^{+0.001}_{-0.001}$

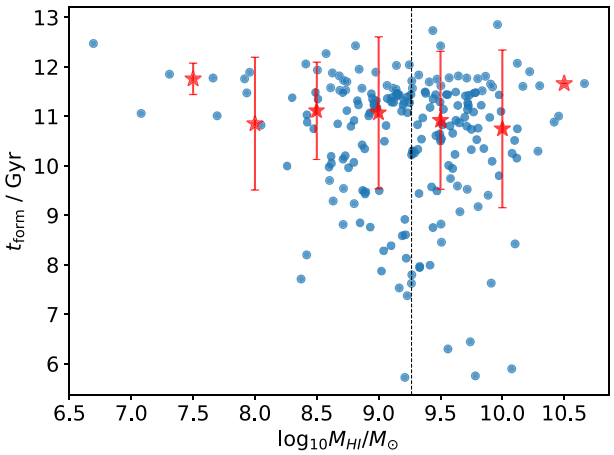

Figure 4. The time of formation $t_{\rm form}$ as a function of the H I mass of a galaxy. The dotted vertical line represents the median $M_{\rm HI}$ value of the sample. The red stars represent the running median of the peak time of star formation $t_{\rm form}$ as a function of $M_{\rm HI}$. The error bars on the running median are calculated by using the standard deviation of the value in each bin. The vertical dotted line represents the mean H I mass of the sample.

between the time a galaxy reached its peak star formation and its stellar mass. This is also confirmed by the correlation tests (Table 4), irrespective of the SFH model (parametric or non-parametric).

The stellar mass of a galaxy being anticorrelated with the time when it reached its peak star formation is not entirely surprising, given the result from the H I-to-stellar mass ratio. It follows that galaxies with higher stellar masses have likely formed stars earlier in their evolution (as can be seen in Fig. 6) and have used up a larger portion of their gas reservoirs. This is essentially a manifestation of cosmic downsizing (L. L. Cowie et al. 1996; G. De Lucia et al. 2006; D. Thomas et al. 2010) whereby the most massive systems formed earlier.

3.2.2 *The gas depletion time-scale of H I-selected galaxies*

The gas depletion time-scale is defined by the ratio of the mass of the gas in a galaxy and the current ongoing SFR. In the case of the H I depletion time-scale, there is obviously an additional link to how quickly the neutral atomic reservoir condenses to form molecular gas from which the stars can form. Nonetheless, it provides a useful indication of how quickly the pristine gas reservoir in the ISM and circumgalactic medium (CGM) is used to fuel star formation.

The atomic H I gas depletion time-scale is simply defined as

$$t_{\rm dep} = \frac{M_{\rm HI}}{\rm SFR}. \quad (5)$$

Similarly to the $t_{\rm form}$ case, we do not find a correlation with H I mass (Fig. 8 for the exponentially delayed parametric model and Fig. 9 for the non-parametric model). The left panel of Fig. 7 shows the atomic gas depletion time $t_{\rm dep}$ as a function of stellar mass for our H I-selected galaxies. As can be seen, lower stellar mass galaxies tend to have significantly longer gas depletion times than their high-H I mass counterparts. This trend is stronger for galaxies with stellar mass $M_\star < 10^{9.5} M_\odot$, and flattens out towards higher masses. This is also confirmed by the correlation tests (Table 5). Given that our galaxies reside on the SF MS, this trend may arise due to a correlation with SFR, and we return to this below. Similarly, in the right-hand side panel of Fig. 7 (or Fig. 11 for the non-parametric case), we show the atomic gas depletion time $t_{\rm dep}$, as a function of the specific star formation rate (sSFR $\equiv$ SFR/$M_\star$). For this case, we do not find a statistically significant link (Table 5).

In Fig. 10, we show the atomic gas depletion time $t_{\rm dep}$ with the H I-to-stellar mass ratio. As can be seen, galaxies with higher H I-to-stellar mass ratios have longer depletion times. This is also confirmed by the correlation tests with both returning statistically significant values (Table 5).

Given the correlations between the atomic gas depletion time and both the stellar mass, the H I-to-stellar mass ratio and the SFR, we investigate which is the dominant parameter that controls the gas depletion time. We therefore perform a partial correlation test (J. T. Macklin 1982; R. A. Johnson, D. W. Wichern & others 2002; J. Whittaker 2009) between the H I mass, the stellar mass and the SFR of the galaxies. We carry out these tests across all combinations of the three parameters. First, for the partial correlation of SFR versus $M_{\rm HI}$ in the presence of $M_\star$ we find the rank coefficient $r = 0.162$, with a p-value of 0.033, thus the correlation between SFR versus $M_{\rm HI}$ is relatively weak, when accounting for stellar mass. Second, for $M_\star$ versus $M_{\rm HI}$ in the presence of SFR, we find a much more significant partial correlation coefficient $r =$

Table 4. The coefficients and *p*-values for the two correlation tests, Kendall's tau and Spearman rank, for each parameter against the $t_{\rm form}$ for the delayed SFH (left) and the non-parametric SFH (right).

Parameter	Delayed SFH				Non-parametric SFH			
	Kendall's tau		Spearman rank		Kendall's tau		Spearman rank	
	τ	*p*-value	Coefficient	*p*-value	τ	*p*-value	Coefficient	*p*-value
$M_{\rm HI}$	−0.05	0.293	−0.077	0.273	−0.148	0.002	−0.21	0.003
$M_\star$	−0.125	0.008	−0.183	0.009	−0.374	0.0	−0.513	0.0
$M_{\rm HI}/M_\star$	0.107	0.023	0.151	0.032	0.34	0.0	0.482	0.0

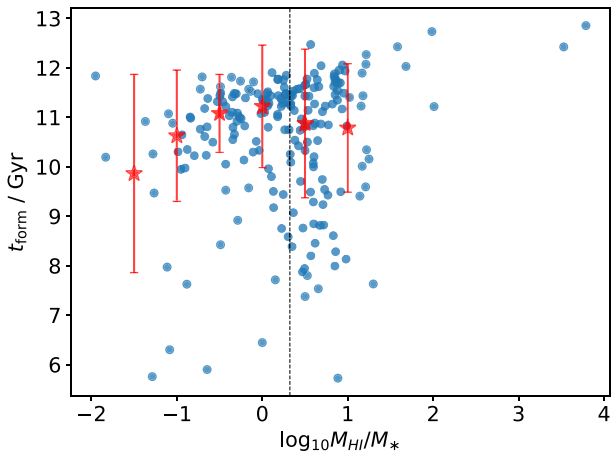

Figure 5. The time of formation $t_{\rm form}$ as a function of the H I-to-stellar mass fraction of a galaxy ($\frac{M_{\rm HI}}{M_\star}$). The red stars represent the running median of the peak time of star formation $t_{\rm form}$ as a function of $M_{\rm HI}/M_\star$. The error bars on the running median are calculated by using the standard deviation of the value in each bin. The vertical dotted line represents the mean H I-to-stellar mass ratio of the sample.

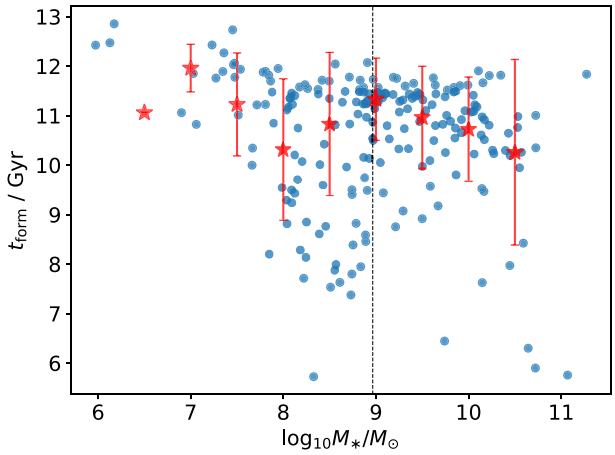

Figure 6. The time of formation $t_{\rm form}$ as a function of the stellar mass $M_\star$ of a galaxy. The red stars represent the running median of the peak time of star formation $t_{\rm form}$ as a function of $M_\star$. The error bars on the running median are calculated by using the standard deviation of the value in each bin. The vertical dotted line represents the mean stellar mass of the sample.

0.54, with a *p*-value of 10^{-14}. Finally for the partial correlation of $M_\star$ versus SFR in the presence of $M_{\rm HI}$, we find a partial correlation coefficient $r = 0.331$, with a *p*-value of 10^{-6}. This implies that the stellar mass is the primary driver for gas depletion time (and the SFR).

We find a clear result that gas-rich galaxies with higher H I mass fractions have longer atomic gas depletion times for an H I-selected sample. This means that they can sustain star formation at their current rate for a longer period of time before their gas is completely depleted. This is consistent with the idea that gas-rich galaxies have a higher potential for ongoing star formation and can replenish their gas reservoirs through accretion from their immediate surroundings (i.e. their CGM; A. E. Jaskot et al. 2015; K. A. Lutz et al. 2017, who also use H I- selected samples in their studies).

The observed correlation between stellar mass and atomic gas depletion time also suggests that more massive galaxies not only have higher gas masses but also exhibit a more efficient utilization of their gas reservoirs for star formation. As dwarf galaxies form in shallower potential wells, the gas will experience a lower gravitational pull, allowing more gas to escape due to the stronger effect of stellar feedback in these galaxies (P. F. Hopkins et al. 2014; M. Romano et al. 2023), or be stripped from it, delaying collapse and preventing efficient replenishment onto the galaxy. This culminates in a less efficient conversion rate from H I to H_2 (L. K. Hunt et al. 2020). Other factors, such as the enhanced susceptibility of the dwarf galaxies to the background UV field (M. Pereira-Wilson et al. 2023), and their overall lower metallicity (C. A. Tremonti et al. 2004) can also reduce the efficiency of the conversion rate. At the other end of the mass scale, the more massive galaxies have a higher density of gas in the central regions that is retained within the deeper potential well, which facilitates star formation (A. Saintonge et al. 2012; V. Parkash et al. 2018; A. Saintonge & B. Catinella 2022).

However, there are some studies which appear to contradict our results. D. Schiminovich et al. (2010) find that the star formation efficiency (SFE $\equiv 1/t_{\rm dep}$), which is the inverse of the depletion time, of massive galaxies in an H I-selected sample to be constant at a value of $10^{-9.5}$ yr^{-1} (for a stellar mass range of $10.0 {\rm M}_\odot < \log_{10} M_\star < 11.5$ M$_\odot$). We note however that this is consistent with our results, as the limited range in stellar mass in the study of D. Schiminovich et al. (2010) means that they would not see the increase (decrease) in gas-depletion time (star formation efficiency) towards lower stellar masses ($M_\star < 10^{10}$ M$_\odot$).

O. I. Wong et al. (2016) find the star-formation efficiency to be constant at $10^{-9.65}$ yr^{-1} across five orders of magnitude of stellar mass (range of 7.0 M$_\odot$ $< \log_{10} M_\star <$ 11.5 M$_\odot$) for star-forming galaxies from the SINGG and SUNGG (G. R. Meurer et al. 2006) surveys. Much of this apparent disagreement can be explained by

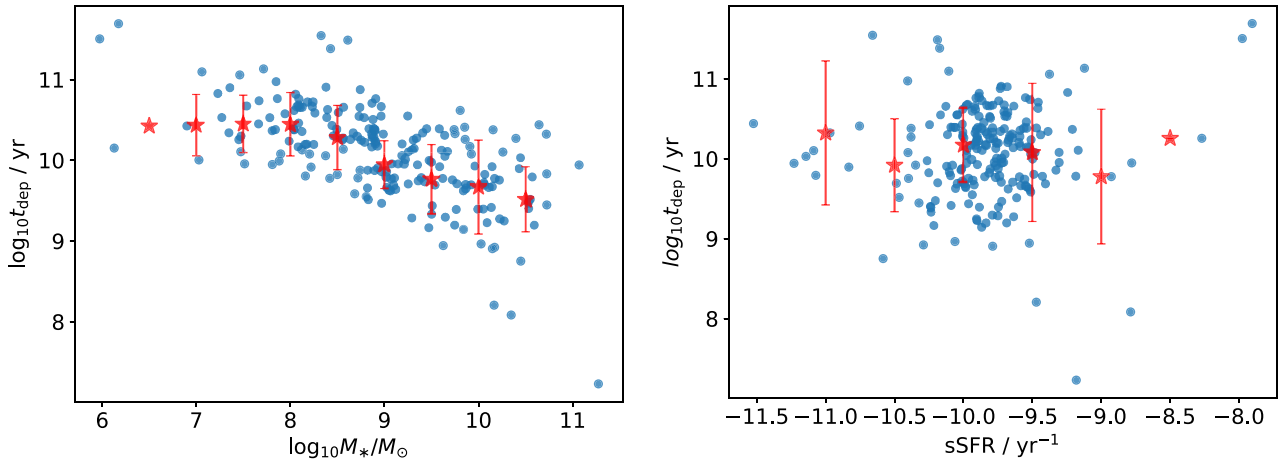

Figure 7. Atomic gas mass depletion $t_{\rm dep}$ as a function of stellar mass $M_\star$ (left) and sSFR (right). The red stars represent the running median of the atomic gas depletion $t_{\rm dep}$ as a function of $M_\star$ (left) and sSFR (right) from the observed MIGHTEE-H I data. The error bars on the running median are calculated by using the standard deviation of the value in each bin.

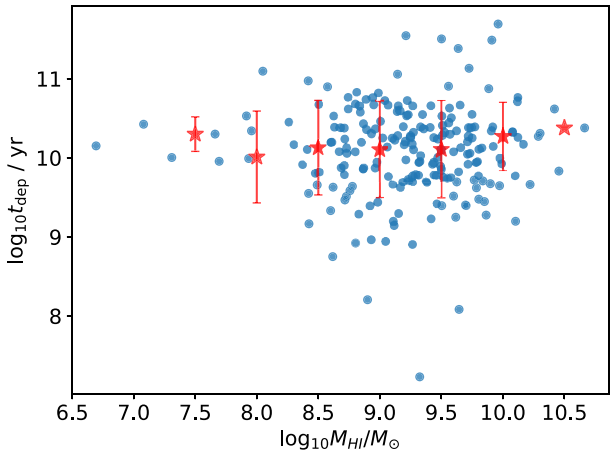

Figure 8. Atomic gas depletion time $t_{\rm dep}$ as a function of $M_{\rm HI}/M_\odot$ for the exponentially delayed SFH. The red stars represent the running median of the atomic gas depletion $t_{\rm dep}$ as a function of $M_{\rm HI}/{\rm M}_\odot$ from the MIGHTEE-H I data. The error bars on the running median are calculated by using the standard deviation of the value in each bin.

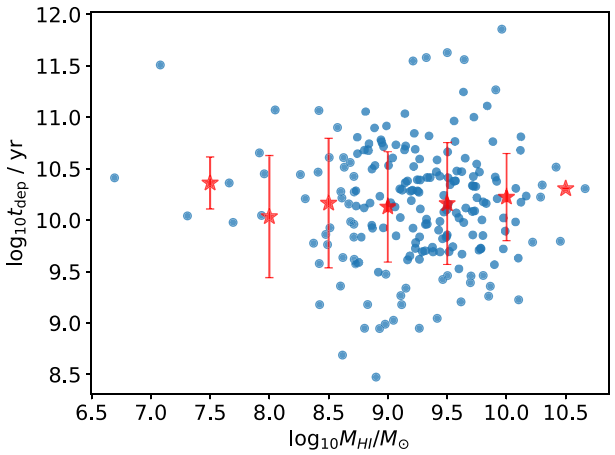

Figure 9. Atomic gas depletion time $t_{\rm dep}$ as a function of $M_{\rm HI}/M_\odot$ for the non-parametric SFH. The red stars represent the running median of the atomic gas depletion $t_{\rm dep}$ as a function of $M_{\rm HI}/{\rm M}_\odot$ from the MIGHTEE-H I data. The error bars on the running median are calculated by using the standard deviation of the value in each bin.

the differing selection criteria, with the galaxies in these studies being stellar mass selected, rather than selected on their atomic gas mass. This is also demonstrated in V. Parkash et al. (2018), who use three different selection criteria for their samples: an H I-selected sample, a spiral galaxy selected sample, and a stellar mass selected sample, which shows that H I-selected samples will result in measurements of high median H I masses and low median SFEs (high median atomic gas depletion times), as opposed to stellar mass selected samples. Indeed, D. Schiminovich et al. (2010); S. Huang et al. (2012) have shown that in the optically selected samples they find on average SFEs which are three times lower than in H I-selected samples.

Returning to our measurement of the atomic gas depletion time, using the left-hand panel of Fig. 7 and restricting our stellar mass range to be closer to the stellar mass ranges in these works (9.0 $\rm M_\odot$ < $\log_{10} M_\star$ < 11.0 $\rm M_\odot$), we find that the $t_{\rm dep}$ trend becomes flatter, with an average SFE of $10^{-9.82\pm0.54}$ $\rm yr^{-1}$. This shows that we are biased towards higher gas depletion times, which is a consequence of using an H I-selected sample. Hence, there is a part of the parameter space (i.e. the bottom left corner in the left-hand panel of Fig. 7) where there is a real lack of galaxies (i.e. we could detect highly star-forming galaxies with low stellar mass and low H I masses if they existed in abundance). This is consistent with these other results, since the H I-selected galaxy sample studies (S. Huang et al. 2014; A. E. Jaskot et al. 2015; K. A. Lutz et al. 2017; Z. Zhou et al. 2018) find a non-constant, increasing SFE (decreasing $t_{\rm dep}$) with increasing stellar mass. On the other hand, stellar-mass or optically selected samples have a large population of low-stellar mass objects and the scatter in the SF MS means that many of these lie above the MS and have already used a significant fraction of their neutral gas reservoir (D. Schiminovich et al. 2010; O. I. Wong et al. 2016). Our sample contains galaxies up to $z = 0.08$

Table 5. The coefficients and *p*-values for the two correlation tests, Kendall's tau and Spearman rank, for each parameter against the t_{dep} for the delayed SFH (left) and the non-parametric SFH (right).

Parameter	Delayed SFH				Non-parametric SFH			
	Kendall's tau		Spearman rank		Kendall's tau		Spearman rank	
	τ	*p*-value	Coefficient	*p*-value	τ	*p*-value	Coefficient	*p*-value
M_{HI}	−0.007	0.874	−0.008	0.91	−0.02	0.67	−0.032	0.653
$M_\star$	−0.446	0.0	−0.633	0.0	−0.451	0.0	−0.622	0.0
$M_{HI}/M_\star$	0.655	0.0	0.827	0.0	0.624	0.0	0.782	0.0
SFR	−0.505	0.0	−0.695	0.0	−0.529	0.0	−0.728	0.0
sSFR	0.039	0.404	0.061	0.388	0.086	0.069	0.126	0.073

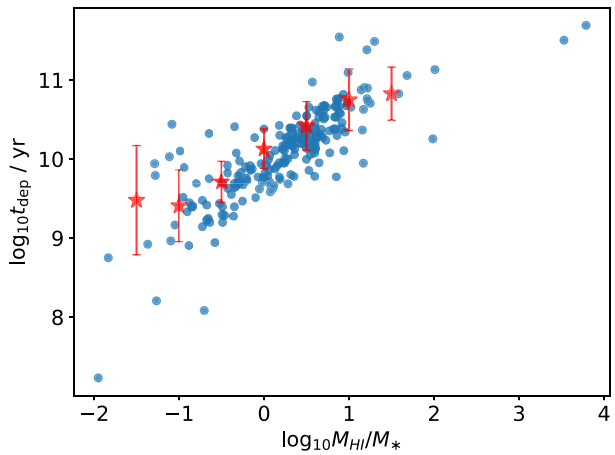

Figure 10. Atomic gas depletion time t_{dep} as a function of $M_{HI}/M_\star$ for the exponentially delayed SFH. The red stars represent the running median of the atomic gas depletion t_{dep} as a function of $M_{HI}/M_\star$ from the MIGHTEE-H I data. The error bars on the running median are calculated by using the standard deviation of the value in each bin.

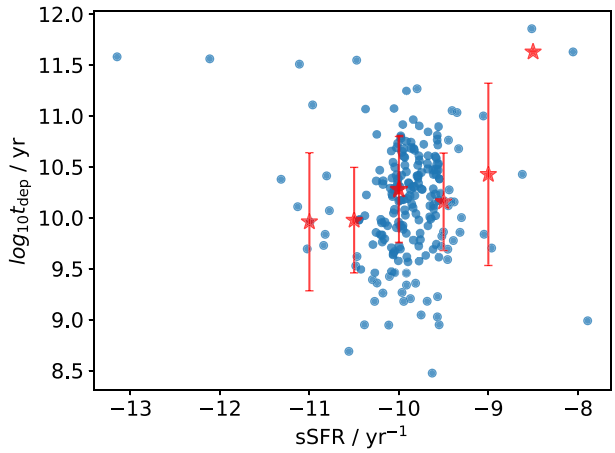

Figure 11. Atomic gas depletion time t_{dep} as a function of sSFR for the non-parametric SFH. The red stars represent the running median of the atomic gas depletion t_{dep} as a function of sSFR from the MIGHTEE-H I data. The error bars on the running median are calculated by using the standard deviation of the value in each bin.

with deep enough multiwavelength data to accurately measure their stellar mass and SFRs, whereas other studies related to the prevalence of H I are either limited in redshift and/or the depth of ancillary data from the UV to the far-infrared. With our sample, we find that for low-stellar-mass ($M_\star \lesssim 10^9$ M$_\odot$) galaxies, the gas depletion time-scale appears to decrease from $M_\star \sim 10^{7.5}$ M$_\odot$ to $M_\star \sim 10^9$ M$_\odot$, whereas for the more massive galaxies ($M_\star > 10^9$ M$_\odot$), the median depletion time appears to be roughly constant.

In order to cross-check these results, we employed the `Simba` simulation (R. Davé et al. 2019). Specifically, we used a 100 Mpc box to generate a mock sample in `Simba` and a 25 Mpc box to generate a mock sample in `Simba`-C, which has an updated chemical enrichment model (R. T. Hough et al. 2023). We matched these samples in M_{HI} using the snapshot closest to the redshifts available in MIGHTEE-H I. Since the mass resolution for `Simba` is 0.725×10^8M$_\odot$, this process resulted in a sample size of 219 sources for each box.

We performed the same statistical tests for t_{dep} on the two simulated samples as we have done for the observed sample. As can be seen in Table 6, we recover the same correlations (or lack of, in the case of M_{HI}) on t_{dep} and M_*, M_{HI}/M_* and SFR. The only one which differs is sSFR, where there is a correlation in the simulated sample which we do not find in the observed one.

3.2.3 *The star-forming main sequence of H I-selected galaxies*

Finally, we look at the SF MS. In Fig. 3, we see that our H I-selected galaxies tend to lie above the $z \sim 0$ galaxy MS, particularly towards higher mass. We also find that the H I mass generally increases with stellar mass, as has been found previously with H I-selected samples (e.g. N. Maddox et al. 2015; H. Pan et al. 2023).

To investigate this further, in Fig. 12 (left) we show the SFR–$M_\star$ plane colour-coded by the deviation from the mean $M_\star$–M_{HI} relation, using Model B from H. Pan et al. (2023) for the mean relation. We find galaxies with a higher positive deviation from the median relation at the lower-mass end of the plot, while galaxies tend to have higher negative deviations at the high stellar mass end, which implies that the high-stellar-mass galaxies in our H I-selected sample are relatively deficient in H I compared to their lower-mass counterparts. This is consistent with the partial correlation results, where we found that between stellar mass, H I mass and SFR, the stellar mass is the main driver of the correlation. Thus, those H I-selected galaxies at $M_\star \gtrsim 10^9$M$_\odot$, which predominantly lie above the MS, have much

Table 6. The coefficients and *p*-values for the two correlation tests, Kendall's tau and Spearman rank, for each parameter against the t_{dep} for the simulated `simba` H I sample (left) and the `simba-C` H I sample (right).

Parameter	Simba				Simba-C			
	Kendall's tau		Spearman rank		Kendall's tau		Spearman rank	
	τ	*p*-value	Coefficient	*p*-value	τ	*p*-value	Coefficient	*p*-value
M_{HI}	0.08	0.08	0.118	0.082	0.068	0.135	0.092	0.174
M_*	0.05	0.273	0.083	0.222	−0.218	0.0	−0.295	0.0
M_{HI}/M_*	0.068	0.137	0.047	0.489	0.357	0.0	0.435	0.0
SFR	−0.471	0.0	nan	nan	−0.499	0.0	nan	nan
sSFR	−0.342	0.0	nan	nan	−0.197	0.0	nan	nan

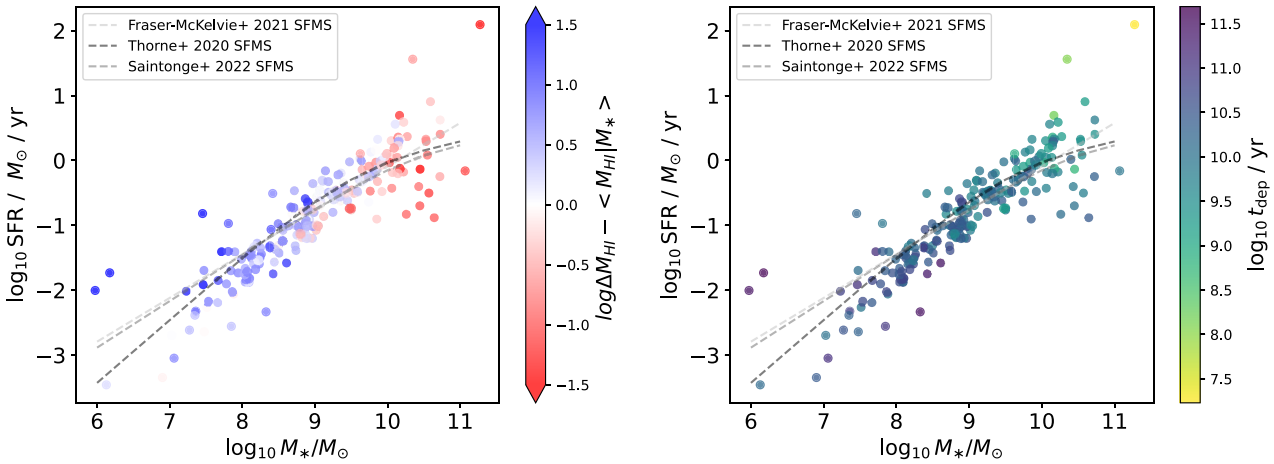

Figure 12. Variations in $\Delta M_{HI} - < M_{HI}|M_\star >$ (left) and t_{dep} (right) across the SFR–$M_\star$ plane. The three dashed lines are different SF-MS fits: the black one is the SF MS as presented in J. E. Thorne et al. (2021), the light grey one is the linear SF MS as presented in A. Fraser-McKelvie et al. (2021), and the dark grey one is the SF MS as presented in A. Saintonge & B. Catinella (2022).

shorter gas depletion time-scales, suggesting that they are using up their gas supply much more efficiently than the galaxies with $M_\star \lesssim 10^9 M_\odot$.

We then used the simulated `Simba`/`Simba-C` samples to compare the SFR–M_* relation to a simulated one. To ensure a fair comparison, we marked the galaxies which could not be represented by the simulation with stars in the SFR–M_* relation, as can be seen in Figs 13 (for the exponentially delayed model) and 14 (for the non-parametric model).

A caveat that has to be included when it comes to `Simba` comparison is that `Simba` is likely overestimating the amount of H I gas in the massive galaxies compared to MIGHTEE-H I. This has been shown in works which model the H I mass function such as H. Pan et al. (2023).

Similarly, low-mass galaxies tend to have a higher atomic gas depletion time t_{dep}, with depletion time decreasing along the MS to high stellar masses. It follows that galaxies with higher stellar masses have likely formed stars earlier in their evolution and have used up a larger portion, but with a significant amount still remaining, of their originally much larger gas reservoirs. This suggests that the most massive galaxies have had a disproportionately large H I reservoir in the past in order to form the current mass in stars. Alternatively, they may have been constantly accreting new gas, as the gas depletion time does not account for this effect. As a galaxy releases both energy and material back into its ISM through processes such as stellar winds, supernova explosions and AGN feedback (e.g. A. Dekel & J. Silk 1986; G. Kauffmann et al. 2003; S. Bertone, G. De Lucia & P. A. Thomas 2007), gas can be heated and expelled into the galaxy's halo or into the CGM. Over time, the outflowing material can cool and condense, transitioning back into gas that falls back towards the galactic disc (J. K. Werk et al. 2014; J. Tumlinson, M. S. Peeples & J. K. Werk 2017). This recycled gas, once reintegrated into the galaxy, can once again form molecular clouds, fuelling new star formation.

However, what is also clear from this figure is that galaxies that begin to drop off from the MS at high masses still retain a significant reservoir of H I, while their SFR is reducing. This suggests a disconnection of the star formation occurring in these galaxies from the availability of neutral atomic hydrogen. Obviously, star formation arises from the cool molecular gas, so the reason for the truncation of star formation relative to a high level of neutral gas could be explained by a reduced efficiency of converting neutral atomic gas to molecular gas, or a reduction in the efficiency of producing stars from the molecular gas reservoir. Several studies have shown that the latter is certainly possible in the highest mass systems, with either significant rotation in the cores of galaxies where the majority of the dense molecular gas resides (e.g. T. A. Davis 2014), or where high velocity dispersion prevents that gas from collapsing (e.g. B. Dey et al. 2019). Such galaxies appear able to retain a significant amount of low-density atomic hydrogen (P. Serra et al. 2012) (see also A. Saintonge & B. Catinella 2022).

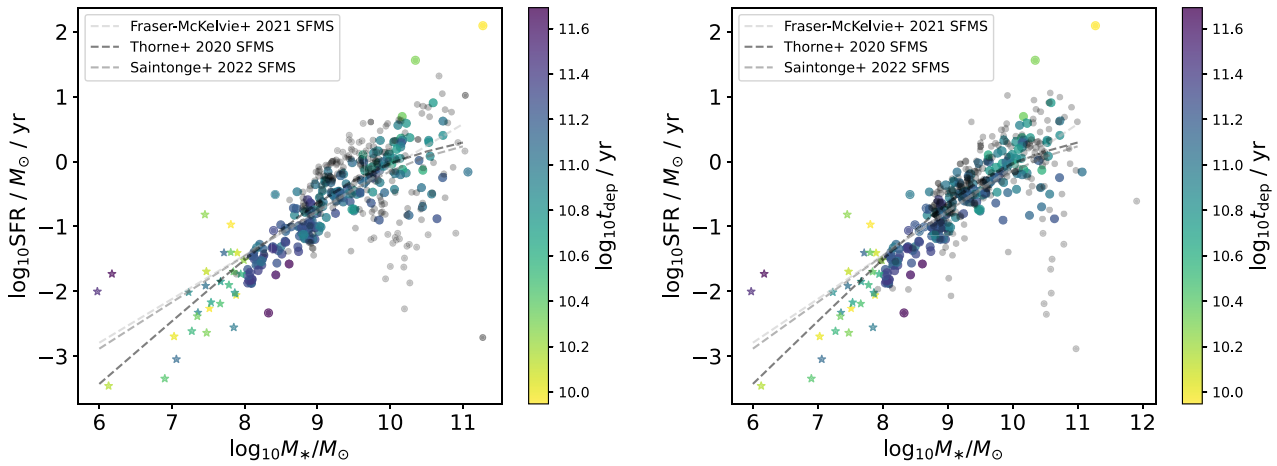

Figure 13. Stellar mass as a function of SFR for the MIGHTEE-H I galaxies with DEVILS cross-match, colour-coded by the depletion time, for the exponentially delayed model. The stars represent the MIGHTEE-H I galaxies below the mass resolution limit of `simba`. The black points show the SFR–M_* from the simulated `Simba` *(left)* and `Simba-C` *(right)* samples.

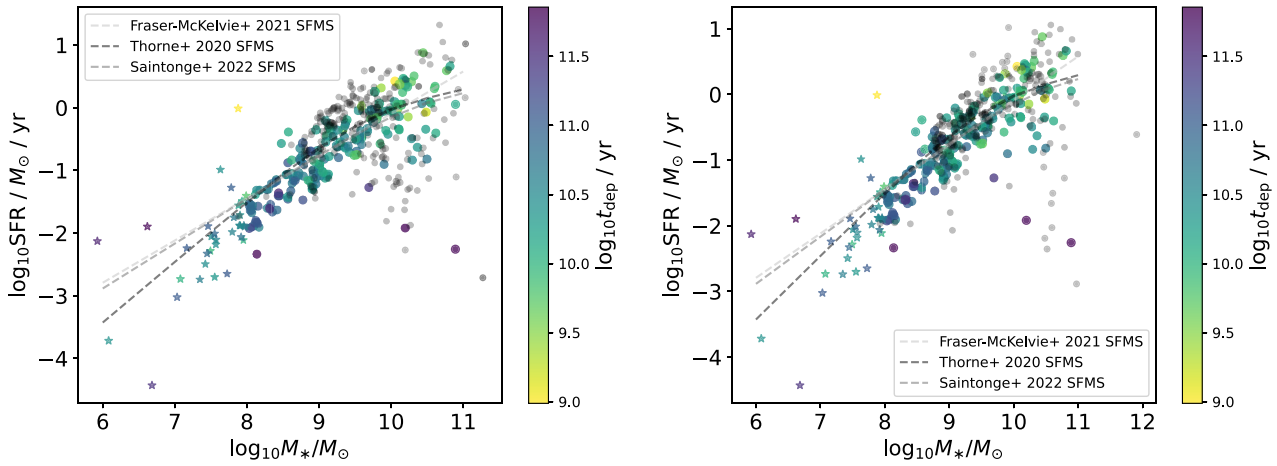

Figure 14. Stellar mass as a function of SFR for the MIGHTEE-H I galaxies with DEVILS cross-match, colour-coded by the depletion time, for the non-parametric model. The stars represent the MIGHTEE-H I galaxies below the mass resolution limit of `Simba`. The black points show the SFR–M_* from the simulated `Simba` *(left)* and `Simba-C` *(right)* samples.

H I-selected galaxies are often found in less dense environments, such as the outskirts of clusters or in the field (i.e. filaments, walls, sheets), where gas stripping processes are less prevalent (L. Verdes-Montenegro et al. 2001; L. M. Walker et al. 2016; M. Crone Odekon et al. 2018; M. G. Jones et al. 2018). This means that the galaxies in an H I-selected sample might be under-represented in dense environments (S. Basilakos et al. 2007; M. J. Meyer et al. 2007; A. M. Martin et al. 2012), i.e. be a biased subset that preferentially retain their gas reservoirs.

Furthermore, as H I extends to larger radii than stars in galaxies, it is more easily perturbed during tidal interactions and hence, more sensitive to external influences that could be caused by the cosmic web (M. S. Yun, P. T. P. Ho & K. Y. Lo 1994; A. Chung et al. 2009). As shown in the section above, we find that the atomic gas depletion time $t_{\rm dep}$ varies with stellar mass. The time-scales it varies across are of order $\sim$ Gyr, as we find an average of $t_{\rm dep} = 6.9$ Gyr across the whole sample. The time for low-redshift galaxies to oscillate across the MS to result in the scatter that is observed has been estimated to be around $\sim$ 5 Gyr (and decreasing for higher redshifts; S. Tacchella et al. 2016). However, our results suggest that the H I reservoir could not respond quickly enough to explain the scatter without external influences or additional physical processes occurring in the galaxies that either trigger or delay star formation. This falls in line with the scenario that the scatter in the MS varies on much longer time-scales, and it is the environment (i.e. the haloes the galaxies reside in, or their position in the cosmic web) that affects how the galaxies move across the MS (J. Matthee & J. Schaye 2019; A. M. Berti et al. 2021). However, the depletion time of a galaxy's gas reservoir and its consumption time are not the same, as the depletion time only accounts for consumption by star formation. In low-mass star-forming galaxies, most simulations suggest strong outflows that can carry out 10−100 times more mass than is forming into stars (D. Nelson et al. 2019; P. D. Mitchell et al. 2020; V. Pandya et al. 2021). This implies that the gas consumption time would be lower than the depletion time by this factor, making the time-scale over which the H I reservoir is consumed to be fairly short,

and suggests that it may be possible for the lower-mass galaxies to vary around the H I MS on ∼Gyr time-scales.

4 CONCLUSIONS

We have fitted the SEDs of 203 galaxies from the MIGHTEE-H I Early Release data with spectroscopic redshifts and excellent multiwavelength photometric data from the FUV to the FIR in order to investigate links between the H I content of galaxies, in the context of an H I-selected sample. By using BAGPIPES, a Bayesian inference-based SED fitting code, we find that most of the galaxies are best described by either a delayed-exponentially declining, a lognormal or an exponentially declining model for the SFHs. We then employed the SED modelling, utilizing the unprecedented wealth of multiwavelength data for an H I-selected sample, to measure the stellar mass, SFR, and the peak time of star formation $t_{\rm form}$, to interpret the process of star formation.

In terms of the H I properties with respect to the SFHs, our main findings are:

(i) We find correlations between the H I-to-stellar mass ratio and the time of formation (positive correlation) and stellar mass and the time of formation (anticorrelation).
(ii) We find positive correlations between the atomic gas depletion time and H I-to-stellar mass ratio and stellar mass of a galaxy.
(iii) We find no correlations between the atomic gas depletion time and the sSFR of a galaxy.

These results are consistent with the picture that lower mass, gas-rich galaxies have a higher depletion time due to a shallower potential well and less efficient star formation, while more massive galaxies have already depleted their gas and formed stars efficiently. This is also reflected in the partial correlation findings, from which we infer that the stellar mass is the main driver. This picture is often seen in H I-selected samples (but not always), so care must be taken when drawing this conclusion. Of note is that this study is carried out at a relatively high redshift for an H I sample and with the ancillary data deep enough to detect galaxies with low stellar mass ($M_\star \sim 10^{7.5}\,{\rm M}_\odot$), with extensive multiwavelength coverage. Most importantly, this persists independent of the SFH model (parametric or non-parametric) used to compute the quantities involved, suggesting the pathway that a galaxy takes to form its stars does not necessarily affect the final correlations. Moreover, due to the time-scales of the atomic gas depletion time, we conclude that the scatter in the SF MS cannot be caused by short time-scale variations, and it has to be caused by long term effects, such as the ones that could be caused by the environment, although we cannot rule out continual short-term expulsion and reintegration of the gas reservoir, particularly in the lower-mass systems.

To investigate this question further, larger samples or more precise spectroscopic data would be required. We will soon have access to far more data from the range of current H I surveys currently underway, but in particular, the wealth of ancillary data over the MIGHTEE fields and the Looking at the Distant University with the MeerKAT Array (LADUMA; S. Blyth et al. 2016) Survey will help elucidate these questions further. Spectroscopy would also provide a different avenue into better constrained SFHs. As such, we could examine the SFHs of galaxies and look for signs of ongoing star formation or merger events by using more accurate measurements of the stellar populations (A. Gallazzi & E. F. Bell 2009; M. Cappellari 2023; A. Nersesian et al. 2024). The forthcoming Wide-area VISTA Extragalactic Surveys (WAVES; S. P. Driver et al. 2019) and specifically the Optical, Radio Continuum and H I Deep Spectroscopic Survey (ORCHIDSS; K. Duncan et al. 2023) will greatly enhance our ability to extract key information for these H I-rich galaxies, while facilitating stacking approaches for stellar-mass or SFR-selected samples.

ACKNOWLEDGEMENTS

MNT, MJJ, IH, SLJ, and HP acknowledge the support of a UKRI Frontiers Research Grant [EP/X026639/1], which was selected by the European Research Council. MNT and MJJ acknowledge support from the Oxford Hintze Centre for Astrophysical Surveys which is funded through generous support from the Hintze Family Charitable Foundation. IH, MJJ, and AAP acknowledge support from the UK Science and Technology Facilities Council [ST/N000919/1]. IH acknowledges support from the South African Radio Astronomy Observatory which is a facility of the National Research Foundation (NRF), an agency of the Department of Science and Innovation. The MeerKAT telescope is operated by the South African Radio Astronomy Observatory, which is a facility of the National Research Foundation, an agency of the Department of Science and Innovation. We acknowledge the use of the Inter-University Institute for Data Intensive Astronomy (IDIA) data-intensive research cloud for data processing. IDIA is a South African university partnership involving the University of Cape Town, the University of Pretoria and the University of the Western Cape. The authors acknowledge the Centre for High Performance Computing (CHPC), South Africa, for providing computational resources to this research project. This work is based on data products from observations made with ESO Telescopes at the La Silla Paranal Observatory under ESO programme ID 179.A-2005 (Ultra-VISTA) and ID 179.A- 2006 (VIDEO) and on data products produced by CALET and the Cambridge Astronomy Survey Unit on behalf of the Ultra-VISTA and VIDEO consortia. Based on observations obtained with MegaPrime/MegaCam, a joint project of CFHT and CEA/IRFU, at the Canada–France–Hawaii Telescope (CFHT) which is operated by the National Research Council (NRC) of Canada, the Institut National des Science de l'Univers of the Centre National de la Recherche Scientifique (CNRS) of France, and the University of Hawaii. This work is based in part on data products produced at Terapix available at the Canadian Astronomy Data Centre as part of the Canada–France–Hawaii Telescope Legacy Survey, a collaborative project of NRC and CNRS. The Hyper Suprime-Cam (HSC) collaboration includes the astronomical communities of Japan and Taiwan, and Princeton University. The HSC instrumentation and software were developed by the National Astronomical Observatory of Japan (NAOJ), the Kavli Institute for the Physics and Mathematics of the Universe (Kavli IPMU), the University of Tokyo, the High Energy Accelerator Research Organization (KEK), the Academia Sinica Institute for Astronomy and Astrophysics in Taiwan (ASIAA), and Princeton University. Funding was contributed by the FIRST program from the Japanese Cabinet Office, the Ministry of Education, Culture, Sports, Science and Technology (MEXT), the Japan Society for the Promotion of Science (JSPS), Japan Science and Technology Agency (JST), the Toray Science Foundation, NAOJ, Kavli IPMU, KEK, ASIAA, and Princeton University.

This research made use of Astropy,[3] a community-developed core Python package for Astronomy (Astropy Collaboration 2013, 2018).

DATA AVAILABILITY

The MIGHTEE-H I spectral cubes will be released as part of the first data release of the MIGHTEE survey, which include cubelets of the sources discussed in this paper (I. Heywood et al. 2022). The derived quantities from the multiwavelength ancillary data were released with the final data release of the VIDEO survey in mid-2021. Alternative products are already available from the Deep Extragalactic VIsible Legacy Survey (DEVILS; L. J. M. Davies et al. 2018).

REFERENCES

Abramson L. E., Gladders M. D., Dressler A., Oemler A. J., Poggianti B., Vulcani B., 2015, ApJ, 801, L12
Adams N. J., Bowler R. A. A., Jarvis M. J., Häußler B., Lagos C. D. P., 2021, MNRAS, 506, 4933
Aihara H. et al., 2019, PASJ, 71, 114
Astropy Collaboration, 2013, A&A, 558, A33
Astropy Collaboration, 2018, AJ, 156, 123
Baldry I. K., Glazebrook K., Brinkmann J., Ivezić Ž., Lupton R. H., Nichol R. C., Szalay A. S., 2004, ApJ, 600, 681
Balogh M. L., Baldry I. K., Nichol R., Miller C., Bower R., Glazebrook K., 2004, ApJ, 615, L101
Barnes J. E., Hernquist L. E., 1991, ApJ, 370, L65
Basilakos S., Plionis M., Kovač K., Voglis N., 2007, MNRAS, 378, 301
Behroozi P. S., Wechsler R. H., Conroy C., 2013, ApJ, 770, 57
Berti A. M., Coil A. L., Hearin A. P., Behroozi P. S., 2021, AJ, 161, 49
Bertone S., De Lucia G., Thomas P. A., 2007, MNRAS, 379, 1143
Blyth S. et al., 2016, in MeerKAT Science: On the Pathway to the SKA. p. 4
Bolzonella M., Miralles J. M., Pelló R., 2000, A&A, 363, 476
Bruzual G., Charlot S., 2003, MNRAS, 344, 1000
Calzetti D., Armus L., Bohlin R. C., Kinney A. L., Koornneef J., Storchi-Bergmann T., 2000, ApJ, 533, 682
Capak P. et al., 2007, ApJS, 172, 99
Cappellari M., 2023, MNRAS, 526, 3273
Cardelli J. A., Clayton G. C., Mathis J. S., 1989, ApJ, 345, 245
Carnall A. C., McLure R. J., Dunlop J. S., Davé R., 2018, MNRAS, 480, 4379
Chabrier G., 2003, PASP, 115, 763
Chung A., van Gorkom J. H., Kenney J. D. P., Crowl H., Vollmer B., 2009, AJ, 138, 1741
Collier J. D., Frank B., Sekhar S., Taylor A. R., 2021, in 2021 XXXIVth General Assembly and Scientific Symposium of the International Union of Radio Science (URSI GASS). IEEE, p. 1
Cook R. H. W. et al., 2024, MNRAS, 531, 708
Cowie L. L., Songaila A., Hu E. M., Cohen J. G., 1996, AJ, 112, 839
Crone Odekon M., Hallenbeck G., Haynes M. P., Koopmann R. A., Phi A., Wolfe P.-F., 2018, ApJ, 852, 142
Croton D. J. et al., 2006, MNRAS, 365, 11
Davé R., Anglés-Alcázar D., Narayanan D., Li Q., Rafieferantsoa M. H., Appleby S., 2019, MNRAS, 486, 2827
Davies L. J. M. et al., 2018, MNRAS, 480, 768
Davies L. J. M. et al., 2021, MNRAS, 506, 256
Davis T. A., 2014, MNRAS, 445, 2378
De Lucia G., Springel V., White S. D. M., Croton D., Kauffmann G., 2006, MNRAS, 366, 499
Dekel A., Mandelker N., 2014, MNRAS, 444, 2071
Dekel A., Silk J., 1986, ApJ, 303, 39
Dey B. et al., 2019, MNRAS, 488, 1926
Di Matteo T., Springel V., Hernquist L., 2005, Nature, 433, 604
Driver S. P. et al., 2019, The Messenger, 175, 46
Duncan K. et al., 2023, The Messenger, 190, 25
Dye S., 2008, MNRAS, 389, 1293
Fabian A. C., 2012, ARA&A, 50, 455
Finlator K., Davé R., 2008, MNRAS, 385, 2181
Fraser-McKelvie A. et al., 2021, MNRAS, 503, 4992
Gallazzi A., Bell E. F., 2009, ApJS, 185, 253
Geha M., Blanton M. R., Masjedi M., West A. A., 2006, ApJ, 653, 240
Glasser G. J., Winter R. F., 1961, Biometrika, 48, 444
Hale C. L. et al., 2024, MNRAS, 536, 2187
Haynes M. P. et al., 2011, AJ, 142, 170
Helmboldt J. F., Walterbos R. A. M., Bothun G. D., O'Neil K., de Blok W. J. G., 2004, ApJ, 613, 914
Heywood I. et al., 2021, MNRAS, 509, 2150
Heywood I. et al., 2022, MNRAS, 509, 2150
Heywood I. et al., 2024, MNRAS, 534, 76
Hildebrand R. H., 1983, QJRAS, 24, 267
Hopkins P. F., Kereš D., Oñorbe J., Faucher-Giguère C.-A., Quataert E., Murray N., Bullock J. S., 2014, MNRAS, 445, 581
Hough R. T., Rennehan D., Kobayashi C., Loubser S. I., Davé R., Babul A., Cui W., 2023, MNRAS, 525, 1061
Huang S., Haynes M. P., Giovanelli R., Brinchmann J., 2012, ApJ, 756, 113
Huang S. et al., 2014, ApJ, 793, 40
Hunt L. K. et al., 2019, A&A, 621, A51
Hunt L. K., Tortora C., Ginolfi M., Schneider R., 2020, A&A, 643, A180
Ilbert O. et al., 2006, A&A, 457, 841
Jarvis M. et al., 2016, in MeerKAT Science: On the Pathway to the SKA. p. 6, preprint (arXiv:1709.01901)
Jarvis M. J. et al., 2013, MNRAS, 428, 1281
Jaskot A. E., Oey M. S., Salzer J. J., Van Sistine A., Bell E. F., Haynes M. P., 2015, ApJ, 808, 66
Jeffreys H., 1998, The Theory of Probability. Oxford Univ. Press
Johnson R. A., Wichern D. W., 2002, Applied Multivariate Statistical Analysis. Prentice-Hall, Upper Saddle River, NJ
Johnston R., Vaccari M., Jarvis M., Smith M., Giovannoli E., Häußler B., Prescott M., 2015, MNRAS, 453, 2540
Jonas J. L., 2009, Proc. IEEE, 97, 1522
Jones M. G. et al., 2018, A&A, 609, A17
Kauffmann G. et al., 2003, MNRAS, 341, 54
Kendall M. G., 1938, Biometrika, 30, 81
Kennicutt Robert C. J., 1998, ARA&A, 36, 189
Kennicutt R. C., Evans N. J., 2012, ARA&A, 50, 531
King A., 2005, ApJ, 635, L121
Lacey C., Cole S., 1993, MNRAS, 262, 627
Leitner S. N., 2012, ApJ, 745, 149
Leja J., Johnson B. D., Conroy C., van Dokkum P. G., Byler N., 2017, ApJ, 837, 170
Leja J., Carnall A. C., Johnson B. D., Conroy C., Speagle J. S., 2019, ApJ, 876, 3
Leslie S. K. et al., 2020, ApJ, 899, 58
Lilly S. J., Carollo C. M., Pipino A., Renzini A., Peng Y., 2013, ApJ, 772, 119
Lonsdale C. J. et al., 2003, PASP, 115, 897
Lutz K. A. et al., 2017, MNRAS, 467, 1083
Macklin J. T., 1982, MNRAS, 199, 1119
Maddox N., Hess K. M., Obreschkow D., Jarvis M. J., Blyth S. L., 2015, MNRAS, 447, 1610
Maddox N. et al., 2021, A&A, 646, A35
Martin A. M., Giovanelli R., Haynes M. P., Guzzo L., 2012, ApJ, 750, 38
Matthee J., Schaye J., 2019, MNRAS, 484, 915
Mauduit J. C. et al., 2012, PASP, 124, 714
McCracken H. J. et al., 2012, A&A, 544, A156
McKee C. F., Ostriker E. C., 2007, ARA&A, 45, 565
McMullin J. P., Waters B., Schiebel D., Young W., Golap K., 2007, in Shaw R. A., Hill F., Bell D. J., eds, ASP Conf. Ser. Vol. 376, Astronomical Data

[3] http://www.astropy.org

Analysis Software and Systems XVI. Astron. Soc. Pac., San Francisco, p. 127
Meurer G. R. et al., 2006, ApJS, 165, 307
Meyer M. J., Zwaan M. A., Webster R. L., Brown M. J. I., Staveley-Smith L., 2007, ApJ, 654, 702
Mitchell P. D., Schaye J., Bower R. G., Crain R. A., 2020, MNRAS, 494, 3971
Muñoz J. A., Peeples M. S., 2015, MNRAS, 448, 1430
Nelson D. et al., 2019, MNRAS, 490, 3234
Nersesian A. et al., 2024, A&A, 681, A94
Noeske K. G. et al., 2007, ApJ, 660, L43
Ocvirk P., Pichon C., Lançon A., Thiébaut E., 2006, MNRAS, 365, 46
Oliver S. J. et al., 2012, MNRAS, 424, 1614
Pacifici C. et al., 2023, ApJ, 944, 141
Pan H. et al., 2023, MNRAS, 525, 256
Pandya V. et al., 2021, MNRAS, 508, 2979
Parkash V., Brown M. J. I., Jarrett T. H., Bonne N. J., 2018, ApJ, 864, 40
Peng Y.-j. et al., 2010, ApJ, 721, 193
Pereira-Wilson M., Navarro J. F., Benítez-Llambay A., Santos-Santos I., 2023, MNRAS, 519, 1425
Ponomareva A. A. et al., 2023, MNRAS, 522, 5308
Popesso P. et al., 2019a, MNRAS, 483, 3213
Popesso P. et al., 2019b, MNRAS, 490, 5285
Robotham A. S. G., Davies L. J. M., Driver S. P., Koushan S., Taranu D. S., Casura S., Liske J., 2018, MNRAS, 476, 3137
Robotham A. S. G., Bellstedt S., Lagos C. d. P., Thorne J. E., Davies L. J., Driver S. P., Bravo M., 2020, MNRAS, 495, 905
Rodríguez-Puebla A., Primack J. R., Behroozi P., Faber S. M., 2016, MNRAS, 455, 2592
Romano M. et al., 2023, A&A, 677, A44
Rosenberg J. L., Schneider S. E., Posson-Brown J., 2005, AJ, 129, 1311
Saintonge A., Catinella B., 2022, ARA&A, 60, 319
Saintonge A. et al., 2012, ApJ, 758, 73
Sanders D. B. et al., 2007, ApJS, 172, 86
Schiminovich D. et al., 2010, MNRAS, 408, 919
Schreiber C. et al., 2018, A&A, 618, A85
Serra P. et al., 2012, MNRAS, 422, 1835
Silk J., Mamon G. A., 2012, Res. Astron. Astrophys., 12, 917
Strateva I. et al., 2001, AJ, 122, 1861
Tacchella S., Dekel A., Carollo C. M., Ceverino D., DeGraf C., Lapiner S., Mandelker N., Primack Joel R., 2016, MNRAS, 457, 2790
Tacchella S. et al., 2022, ApJ, 926, 134
Taylor A. R. et al., 2024, MNRAS, 528, 2511
Thomas D., Maraston C., Schawinski K., Sarzi M., Silk J., 2010, MNRAS, 404, 1775
Thorne J. E. et al., 2021, MNRAS, 505, 540
Tremonti C. A. et al., 2004, ApJ, 613, 898
Tumlinson J., Peeples M. S., Werk J. K., 2017, ARA&A, 55, 389
Verdes-Montenegro L., Yun M. S., Williams B. A., Huchtmeier W. K., Del Olmo A., Perea J., 2001, A&A, 377, 812
Walcher J., Groves B., Budavári T., Dale D., 2011, Ap&SS, 331, 1
Walker L. M., Johnson K. E., Gallagher S. C., Privon G. C., Kepley A. A., Whelan D. G., Desjardins T. D., Zabludoff A. I., 2016, AJ, 151, 30
Werk J. K. et al., 2014, ApJ, 792, 8
Whitaker K. E., van Dokkum P. G., Brammer G., Franx M., 2012, ApJ, 754, L29
Whitaker K. E. et al., 2014, ApJ, 795, 104
Whitaker K. E. et al., 2015, ApJ, 811, L12
Whittaker J., 2009, Graphical Models in Applied Multivariate Statistics. Wiley
Wong O. I., Meurer G. R., Zheng Z., Heckman T. M., Thilker D. A., Zwaan M. A., 2016, MNRAS, 460, 1106
Yun M. S., Ho P. T. P., Lo K. Y., 1994, Nature, 372, 530
Zamojski M. A. et al., 2007, ApJS, 172, 468
Zhou Z., Wu H., Zhou X., Ma J., 2018, PASP, 130, 094101

SUPPORTING INFORMATION

Supplementary data are available at *MNRAS* online.

MIGHTEE_HI_ES_delayed_sfh_params.fits

Please note: Oxford University Press is not responsible for the content or functionality of any supporting materials supplied by the authors. Any queries (other than missing material) should be directed to the corresponding author for the article.

APPENDIX A: EXAMPLES OF FITS AND CORNER PLOTS

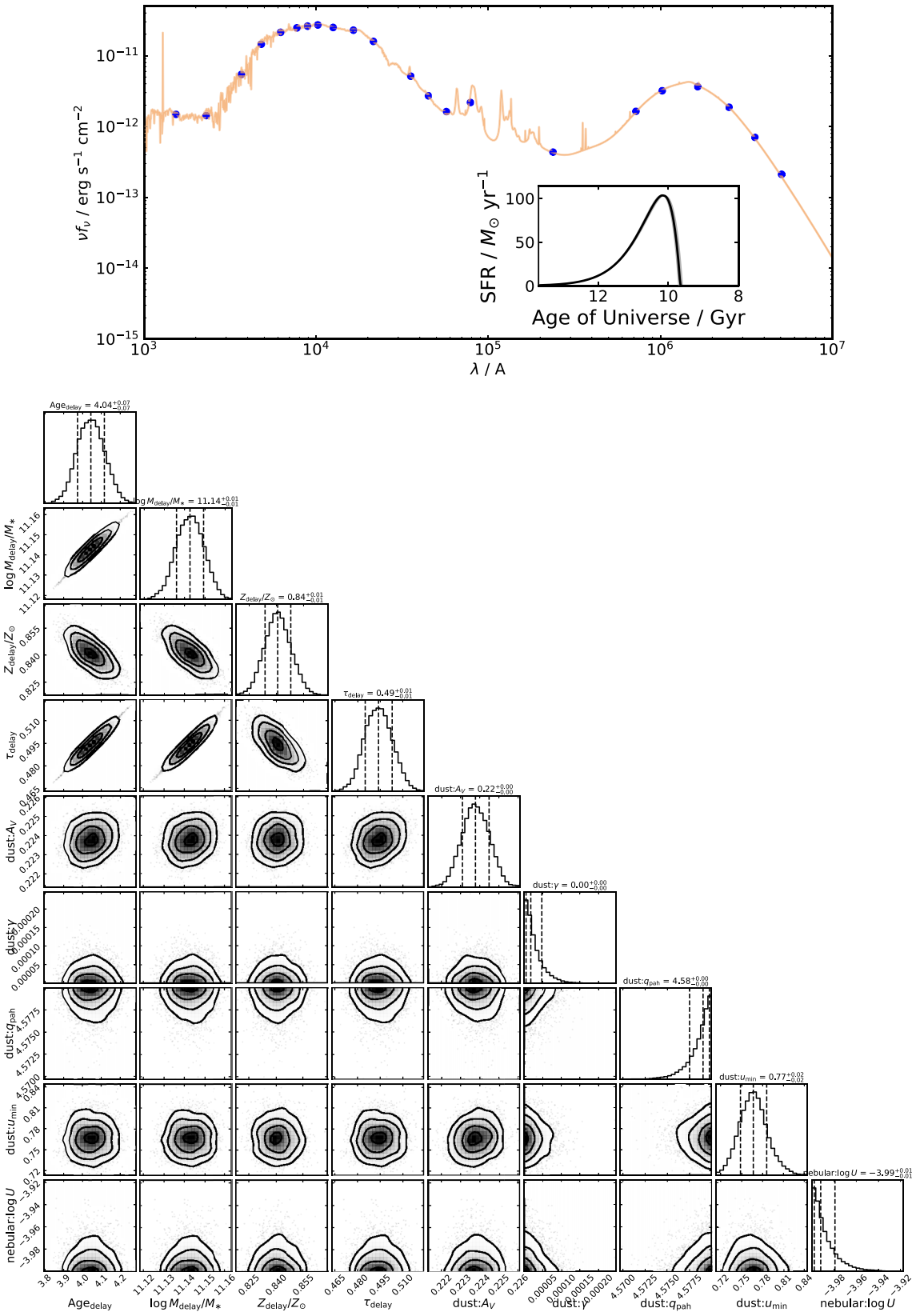

Figure A1. An example of the photometric output of one of the MIGHTEE-H I Early Science galaxies using the available photometric filters (*top*) and a corner plot (*bottom* of one of the MIGHTEE-H I Early Science galaxies (Galaxy ID 82, a massive galaxy with $M_\star = 10^{10.86}$ M$_\odot$ and SFR of 0.7M$_\odot$/yr) using the available photometric filters, fitted with an exponentially delayed SFH model.

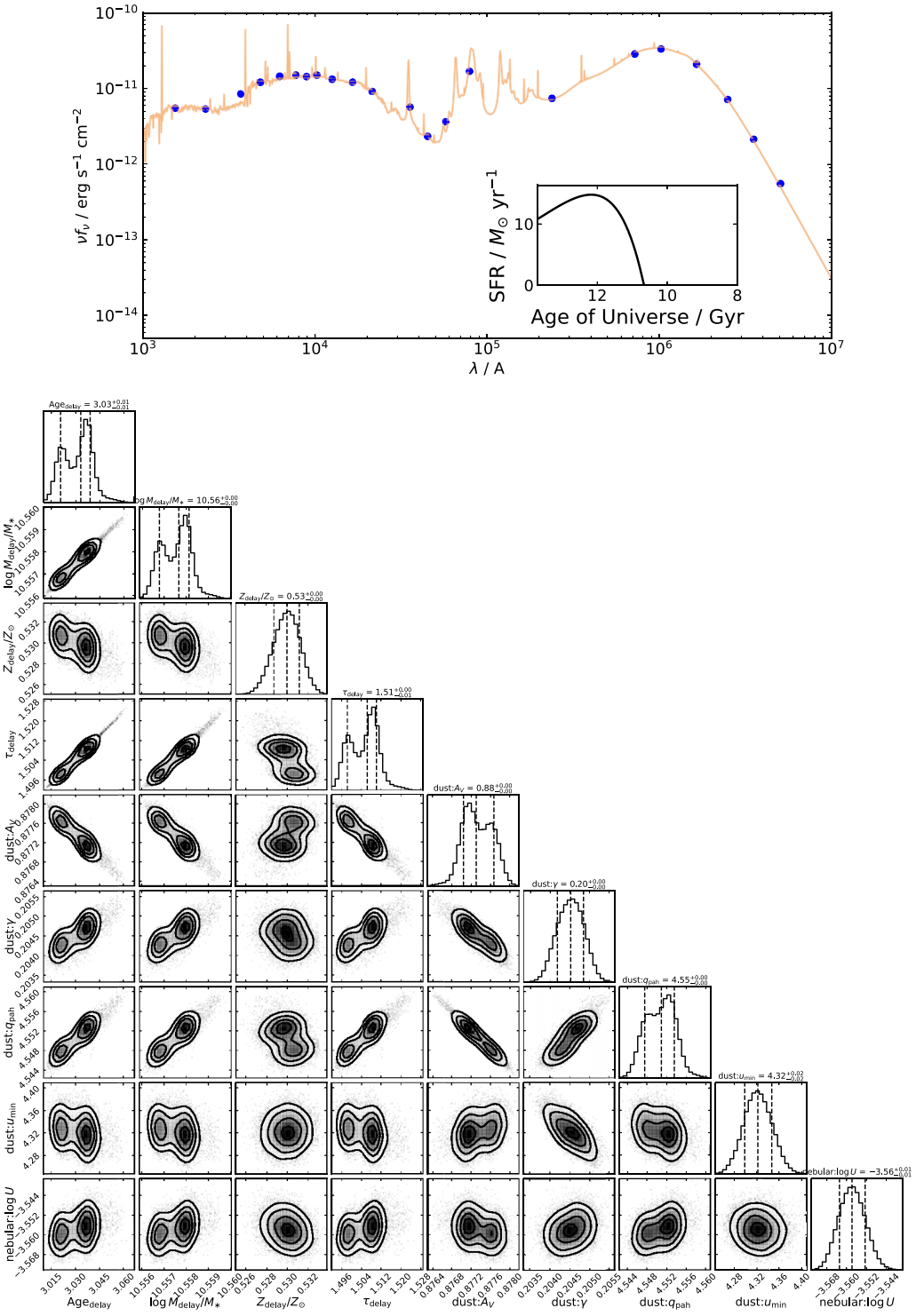

Figure A2. An example of the photometric output of one of the MIGHTEE-H I Early Science galaxies using the available photometric filters (*top*) and a corner plot (*bottom* of one of the MIGHTEE-H I Early Science galaxies (Galaxy ID 158, the galaxy with the highest SFR in the sample and $M_\star = 10^{10.28}$M$_\odot$) using the available photometric filters, fitted with an exponentially delayed SFH model.

This paper has been typeset from a TEX/LATEX file prepared by the author.